A&A, 706, A302 (2026)
https://doi.org/10.1051/0004-6361/202557017

Astronomy & Astrophysics

JWST-discovered AGN: Evidence of heavy obscuration in the type 2 sample from the first stacked X-ray detection

A. Comastri[1,⋆], G. Lanzuisi[1], F. Vito[1], S. Marchesi[2,1,3], M. Brusa[2,1], R. Gilli[1], I. Juodžbalis[4,5], R. Maiolino[4,5,6], G. Mazzolari[7,1], G. Risaliti[8,9], J. Scholtz[4,5], and C. Vignali[2,1]

[1] INAF – Osservatorio di Astrofisica e Scienza dello Spazio di Bologna (OAS), Via Gobetti 93/3, I-40129 Bologna, Italy
[2] Dipartimento di Fisica e Astronomia (DIFA), Università di Bologna, Via Gobetti 93/2, I-40129 Bologna, Italy
[3] Department of Physics and Astronomy, Clemson University, Kinard Lab of Physics, Clemson, SC 29634, USA
[4] Kavli Institute for Cosmology, University of Cambridge, Madingley Road, Cambridge CB3 OHA, UK
[5] Cavendish Laboratory – Astrophysics Group, University of Cambridge, 19 JJ Thomson Avenue, Cambridge CB3 OHE, UK
[6] Department of Physics and Astronomy, University College London, Gower Street, London WC1E 6BT, UK
[7] Max-Planck-Institut für extraterrestrische Physik (MPE), Gießenbachstraße 1, 85748 Garching, Germany
[8] Dipartimento di Fisica e Astronomia, Università di Firenze, Via G. Sansone 1, I-50019 Sesto Fiorentino, Firenze, Italy
[9] INAF – Osservatorio Astrofisico di Arcetri, Largo Enrico Fermi 5, I-50125 Firenze, Italy

Received 28 August 2025 / Accepted 21 December 2025

ABSTRACT

One of the most puzzling properties of the high-redshift active galactic nucleus (AGN) population recently discovered by JWST, including both broad-line and narrow-line sources, is their X-ray weakness. With very few exceptions, and regardless of the optical classification, they are undetected at the limits of the deepest Chandra fields, even when stacking signals from tens of sources in standard observed-frame energy intervals (soft, hard, and full bands). It has been proposed that their elusive nature in the X-ray band is due to heavy absorption by dust-free gas or an intrinsic weakness, possibly due to high super-Eddington accretion. For this work we performed X-ray stacking in three customized rest-frame energy ranges (1–4, 4–7.25, and 10–30 keV) of a sample of 50 type 1 and 38 type 2 AGN identified by James Webb Space Telescope (JWST) in the Chandra Deep Field South (CDFS) and Chandra Deep Field North (CDFN) fields. For the type 2 subsample, we achieve a total exposure of about 210 Ms, and report a significant detection ($\sim 3\sigma$) in the hardest band (10–30 keV rest frame), along with relatively tight upper limits in the rest-frame softer energy bands. The most straightforward interpretation is in terms of heavy obscuration due to gas column densities well within the Compton-thick regime ($>2 \times 10^{24}$ cm^{-2}) with a large covering factor, approaching 4π. The same procedure applied to the type 1 subsample returns no evidence of a significant signal in about 140 Ms stacked data in any of the adopted bands. The bolometric correction $k_{\rm bol}$ to the absorption corrected 2–10 keV X-ray luminosity of type 2 AGN is consistent with the average value obtained for X-ray selected type 2 objects in the literature. The lower limit on $k_{\rm bol}$ for the type 1 sample is significantly higher and inconsistent with that of type 2 objects. Absorption in the Compton-thick regime or extreme X-ray weakness, would bring the current lower limits closer to the observed values for type 1 X-ray selected AGN. A brief comparison with the current observations and the implications for the evolution of AGN are discussed.

Key words. galaxies: active – galaxies: high-redshift – quasars: general – quasars: supermassive black holes

1. Introduction

Several surveys with the James Webb Space Telescope (JWST) have discovered a population of high-redshift ($z \sim 4-10$) active galactic nuclei (AGN) with bolometric luminosities significantly lower ($<10^{45}$ erg s^{-1}) than previously observed in bright quasars dominating the AGN population at high redshift. Most of them have been identified via the detection of relatively broad emission lines with Hα widths on the order of 2000 km s^{-1}, and are thus classified as type 1 AGN (e.g., Maiolino et al. 2024b, Juodžbalis et al. 2025, hereafter J25). Their black hole mass estimates range from 10^6 to 10^8 M$_\odot$ (e.g., Maiolino et al. 2024a; Kocevski et al. 2023). They tend to be over-massive compared to the stellar masses of their host galaxies, and with respect to the local relation, suggesting a vigorous growth phase at early times (although this interpretation is still debated; see Ananna et al. 2024). About 10–30% of them (Hainline et al. 2025) are dubbed little red dots owing to their point-like appearance and red near-infrared colors; in addition to broad permitted lines, they are characterized by a V-shaped continuum, with a relatively blue UV slope (e.g., Kocevski et al. 2025). Additionally, a growing number of narrow-line type 2 AGN are identified using several diagnostic diagrams for the emission line, some specifically developed for the classification of the emission lines at high redshift (Scholtz et al. 2025; Mazzolari et al. 2025; Calabrò et al. 2023). The space densities of these newly JWST-discovered AGN at $z \sim 4-6$ are about one to two orders of magnitude higher than the extrapolation of the quasars luminosity function and of the X-ray selected AGN luminosity function (e.g., Harikane et al. 2023; Matthee et al. 2024; Greene et al. 2024; Maiolino et al. 2024a; Juodžbalis et al. 2025) suggesting that JWST is tracing the emergence of a new population that is much larger than the most optimistic (Giallongo et al. 2015) estimates from the X-ray-selected AGN. Given that known X-ray-emitting AGN account for some 80–90% of the X-ray background (e.g., Moretti et al. 2003; Cappelluti et al. 2017), it is

⋆ Corresponding author: andrea.comastri@inaf.it

not surprising that this new population is X-ray silent. Although many examples of X-ray weak quasars were reported in the literature (Risaliti et al. 2001) well in advance the JWST surveys, the JWST population is much larger. Even more intriguing, this new population remains undetected even with stacking techniques performed in deep X-ray observations such as those in the Chandra Deep Fields (Yue et al. 2024, Mazzolari et al. 2024, Maiolino et al. 2025, hereafter, M25).

Two broad classes of models were proposed to explain the X-ray weakness. The first is super-critical accretion resulting in an extremely soft X-ray spectrum (e.g., Pacucci & Narayan 2024; Madau & Haardt 2024; Madau 2025; Maiolino et al. 2025) and significant absorption at high inclinations due to self-shadowing. The second class is heavy obscuration with a high covering factor and column densities exceeding 10^{24} cm^{-2} by dust free–poor gas to account for the presence of broad lines and UV emission (e.g., M25, Ji et al. 2025, Juodžbalis et al. 2024).

In the first case, the steep X-ray emission explains the lack of detection in the observed standard (0.5−2 and 2−7 keV) bands corresponding, approximately, to 4–40 keV rest frame. The heavy absorption hypothesis implies that the X-ray flux is dimmed by obscuration, especially in the soft band. For optical depths on the order of $\tau \gg 1$ and large covering factors, the signal in the hard X-ray band may also be strongly suppressed.

In order to understand which physical mechanism is more likely to explain the observed properties, we carried out a *Chandra* stacking analysis at the positions of the sources in our sample in several energy intervals, tuned to detect characteristic features of heavy absorption, such as a very hard X-ray spectrum emerging at >8 keV, enhanced emission around the iron line complex at ∼6−7 keV and–or the presence of a strong soft excess below about 1 keV. A detection in the stacked signal in the softest energy channels would be suggestive of a steep spectrum, possibly related to supercritical accretion, while a signal at the hardest energies would favor the heavy obscuration interpretation. In principle, it is possible to constrain the average column densities, owing to the strong dependence of the X-ray flux upon the optical depth for Compton scattering. The present work takes a step further with respect to previous analyses based on the search for a stacked signal in deep *Chandra* fields as we explicitly stack emission from all sources in the samples in the same rest-frame bands, and fully exploit the stacked X-ray SED shapes to estimate the absorption levels.

The paper is organized as follows. In Section 2 the sample selection is presented. In Section 3 we describe the procedure adopted to analyze (stack) the X-ray data. In Section 4 we present our results. In Section 5 we discuss the implications of our results in light of the current models of the X-ray and multiband properties of JWST AGN and draw our conclusions. Errors and upper limits are reported at the 68% confidence level, while the upper limits in Figure 5 are given at the 90% confidence. We adopt a flat cosmology with $H_0 = 67.7\,\mathrm{km\,s^{-1}}$ and $\Omega_m = 0.307$ (Planck Collaboration XIII 2016).

2. The JWST sample of AGN

Our parent sample is composed of AGN identified by JWST in the footprints of the GOODS-N and GOODS-S fields, the deepest *Chandra* fields, with a total exposure of about 2 and 7 million seconds, respectively. The choice is dictated by the need for deep X-ray exposures to obtain meaningful limits on the AGN X-ray emission. The optical classification as type 1 and type 2 AGN is mainly from the JWST Advanced Deep Extragalactic Survey (JADES; Eisenstein et al. 2025, D'Eugenio et al. 2025).

The type 1 AGN were identified based on the broad component in the Hα and Hβ emission with a full width at half maximum (FWHM) $> 1000\,\mathrm{km\,s^{-1}}$ (Matthee et al. 2024), without a corresponding kinematical component in the [OIII] $\lambda\lambda$5007,4960, hence ruling out an outflow origin. In total, this work yields a clean selection of 35 type 1 AGN in the GOODS-S and GOODS-N fields. We also considered the type 1 objects from the First Reionization Epoch Spectroscopically Complete Observations (FRESCO) survey (Oesch et al. 2023), the two little red dots at $z > 7$ in Xiao et al. (2025), and the broad Hα emitters in the JADES, FRESCO, and Complete NIRCam Grism Redshift Survey (CONGRESS) surveys selected by Zhang et al. (2025). The type 1 objects are published in J25 and also in M25. We refer to the discovery papers for further details on the selection and classification.

The type 2 AGN were selected from Scholtz et al. (2025), which is a pilot study to select type 2 AGN in the JADES survey. As such, it was only employed on the first two tiers of JADES observations, at that point only observed in GOODS-S. The emission line diagnostics used in the pilot study were the Baldwin et al. (1981) and Veilleux & Osterbrock (1987) diagrams, with selection criteria modified for high-z by Scholtz et al. (2025) to account for low-metallicity star formation, the HeII λ4686 diagrams (Shirazi & Brinchmann 2012), UV emission line diagnostics (Hirschmann et al. 2019), and the presence of high-ionization lines such as [NeIV] λ2424 and [NeV] λ3420. In total, this study selected 41 unique type 2 AGN in the regions of the GOODS-South field from a total of 209 galaxies covering the redshift range 2–9.5. The full selection of type 2 AGN from the JADES survey that will cover the GOODS-N field will be presented in Scholtz et al. (in preparation). The list of sources is reported in the Appendix in Tables A.1 (type 1) and A.2 (type 2). We only used the robust AGN candidate in the Chandra Deep Field South CDFS from J25 and removed the tentative candidates from our sample.

The sources' X-ray emission is discussed in M25 and J25. A few sources were detected in the X-ray band and excluded from our sample. Two broad-line AGN (GN 721 and XID_403[1]) are relatively faint in the X-rays ($k_{\mathrm{bol},X} > 100$, where $k_{\mathrm{bol},X} = L_{\mathrm{bol}}/L_{2-10\,\mathrm{keV}}$), but with a hard X-ray spectrum consistent with Compton-thick obscuration (Gilli et al. 2014; Circosta et al. 2019). The absorption-corrected bolometric correction derived from Compton-thick obscuration is consistent with the observed distribution of standard type 1 AGN. Two additional broad-line AGN (GS_49729 and GS_209777) were detected with an unobscured X-ray spectrum ($\Gamma \sim 1.7$) and average bolometric correction $k_{\mathrm{bol},X} \sim 15$, hence also consistent with standard type 1 AGN. One type 2 object (GS_21150) was X-ray detected, but with an insufficient number of photon counts to estimate the spectral shape. In the following, we consider the 38 type 2 and 50 type 1 AGN that are not individually detected, and that do not produce a significant stacked signal in the standard observed-frame soft (0.5–2 keV) and hard (2–7 keV) *Chandra* bands (M25).

The relevant data for the two samples are reported in Appendix A, and in Tables A.1 and A.2. The redshift distributions for the two samples are reported in the two panels of Figure 1. As a consequence of the JADES parent sample's selection criteria, most sources are at $z > 2$, extending up to $z \sim 9$. The median redshifts are $z \sim 4.2$ for type 2 and $z \sim 5$ for type 1.

For type 2 AGN, the bolometric luminosity is inferred from the extinction-corrected [O III]5007 line, adopting the scaling

[1] The ID refers to the *Chandra* 4 Ms catalog (Xue et al. 2011).

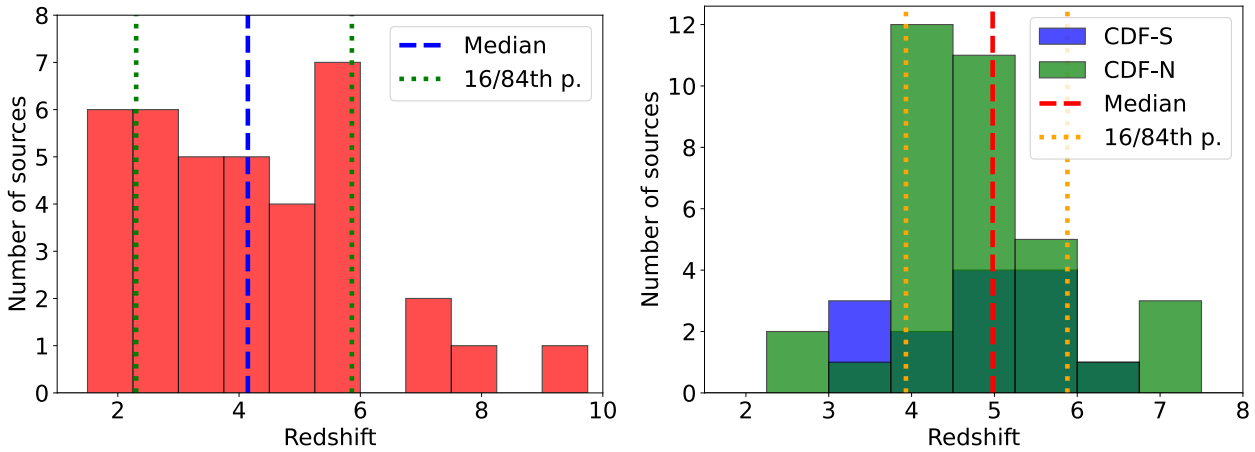

Fig. 1. Left: Redshift distribution for the type 2 AGN analyzed in this work, all from CDF-S. The median of the distribution is reported, as well as the 16th and 84th percentiles, as labeled. Right: Redshift distribution for the type 2 AGN analyzed in this work, from the CDF-S (blue) and CDF-N (green). The median of the distribution is reported, as well as the 16th and 84th percentiles, as labeled.

relation given in S25, and is reported in Table A.2 and Figure 6 (left). As can be seen in the figure, the bolometric luminosities span more than three orders of magnitude in the range $\log \frac{L_{\rm bol}}{\rm erg\,s^{-1}} \sim 41.5{-}45.0$.

For type 1 AGN, the bolometric luminosity is inferred from the Hα luminosity, adopting the scaling relation provided by Stern & Laor (2012), and is reported in Table A.1. The bolometric luminosities of type 1 cover about three orders of magnitude, in a significantly higher $L_{\rm bol}$ interval with respect to type 2 AGN $\left(\log \frac{L_{\rm bol}}{\rm erg\,s^{-1}} \sim 43{-}46\right)$. Figure 6 (right) only shows the type 1 AGN from M25, for which we have a direct estimate of the $k_{{\rm bol},X}$.

The 38 type 2 AGN from S25 all lie in the CDFS, within 3.3 arcmin from the field center. Thus, we took advantage of the sharpest *Chandra* psf (90% encircled counts fraction always within 2.5 arcsec radius). The type 1 AGN in the Chandra Deep Field North (CDFN, 36 sources) lie in the central region of the field, within 3–4 arcmin of the aimpoint of the majority of the pointings, thus contributing to the total 2Ms exposure. Half of the type 1 AGN in the CDFS (7 sources) lie in the central 3 arcmin region of the field, while the other half are selected from different JWST pointings and are located between 4 and 7 arcmin (90% encircled counts fraction goes from 3 to 6 arcsec radius).

3. Data reduction and stacking procedure

To increase the sensitivity of the X-ray stacking analysis, we performed a stack in three adaptively chosen bands to test the hypothesis of heavy obscuration in the average spectrum of the sources in the sample.

The X-ray data in the *Chandra* deep fields were reduced and extensively analyzed by many authors. For the present paper, we rely on the data products (e.g., stacked event files, exposure maps, source catalogs) made available by the Penn State *Chandra* team[2]. We refer to Luo et al. (2017) and Xue et al. (2016) for all the details of the *Chandra* data analysis.

In order to obtain a robust estimate of the background, the detected sources from the Luo et al. (2017) catalog were removed from the event files, assuming circular regions whose radius is a function of the source intensity: from 4 pixels (2″) for <30 full band counts to 6 pixels (3″) for bright >100 counts sources. The adopted radii exclude 95–98% of the counts of the detected sources. This ensures <1 count per source on average, leaking outside the excluded region. The local background was estimated in a box of 20 pixels on each side around the excluded regions. The masked pixels were then assigned random discrete values extracted from a Poisson distribution with the expectation value set to the median background counts per pixel, thus reproducing the same background levels. For each source to be stacked, square cutouts of 50 pixels were created around the input position.

The novelty of our approach with respect to previous works that stacked Chandra images at the position of known JWST sources lies in the careful selection of the energy bands where the stacking is performed. Specifically, we selected three rest-frame bands (1–4, 4–7.25, and 10–30 keV), corresponding to different observed bands depending on the redshift of each source included in the stacking. In the rest of the paper we refer to these bands as the soft band (SB, 1–4 keV), medium band (MB, 4–7.5 keV), and ultra-hard band (UHB, 10–30 keV). The 1–4 keV band was chosen to include the softest photons detectable by Chandra in the observed energy range, while we chose the 10–30 keV band as our hardest band after performing multiple tests[3] that allowed us to determine that such an energy range is the best trade-off between the band width, to maximize the total counts, and the high-energy boundary, to minimize the background counts. We limited the MB to 7.25 keV, a trade-off between the band width and the expected spectral shape, which drops quickly, especially for obscured sources, above the iron K-edge.

The total stacked counts (Table 1) are extracted from a circular region centered at the optical JWST position with $R = 2''$, whereas the background counts are measured from an annular region with inner radius of 5″ and outer radius of 10″ and then rescaled for the background-to-source area ratio. The net source counts are then computed by subtracting the rescaled background counts from the total counts. The errors are propagated accordingly.

[2] Available at https://personal.science.psu.edu/wnb3

[3] The other bands we tested are the 8–20 keV, 8–30 keV, and 10–20 keV ones.

Table 1. Stacking results for the type 1 and type 2 samples.

Sample	T_{exp} [Ms]		Total Counts SB	MB	UHB
Type 1	139.8	SRC	<11.4	<12.2	<34.6
		BKG	125.6 ± 2.6	148.1 ± 2.8	639.5 ± 5.9
Type 2	209.4	SRC	<16.6	<41.7	122.8 ± 38.3
		BKG	263.8 ± 3.8	295.5 ± 4.0	1272.2 ± 8.3

Notes. Total and background counts in the SB, MB, and UHB. The source counts are net counts. The background counts are scaled to the size of the source region. The type 1 exposure is 59.6 Ms for CDFN and 80.2 Ms for CDFS.

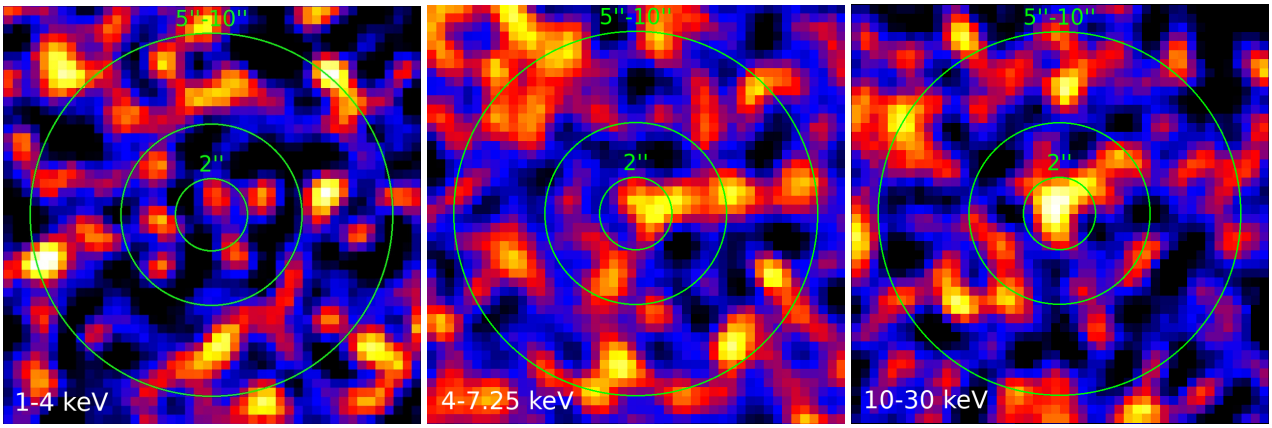

Fig. 2. Left: Type 2 stacked image 1–4 keV rest frame. Center: Type 2 stacked image 4–7.25 keV rest frame. Right: Type 2 stacked image 10–30 keV rest frame.

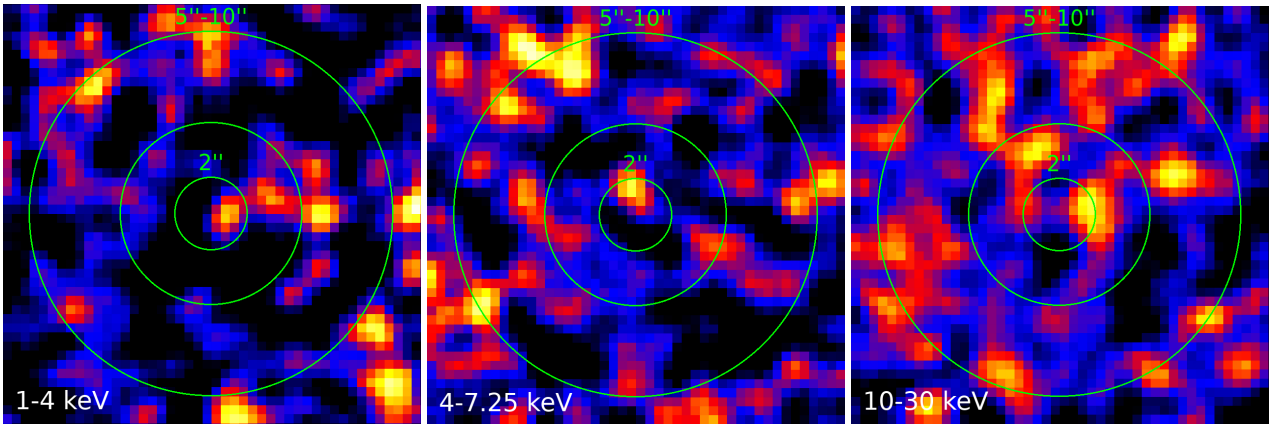

Fig. 3. Total (CDFS + CDFN) stacked images for the type 1 sample. Left: 1–4 keV SB. Center: 4–7.25 keV MB. Right: 10–30 keV UHB.

4. Results

The thumbnails associated with the rest-frame stack in the SB, MB, and UHB bands are shown in Figure 2 and Figure 3 for the type 2 and type 1 AGN, respectively. The background and source counts for both samples are reported in Table 1.

The AGN in the type 1 sample were not detected in any rest-frame bands. The sources in the type 2 AGN sample were not detected in the SB and MB (as defined above), while they were detected in the UHB, with significance $(1 - P_B) = 0.9996$ using Poisson statistics (0.9993 with Gaussian statistics). We also considered the possibility that the UHB signal is due to a specific subset of sources. Several tests were performed by dividing the type 2 sample according to their redshift, bolometric luminosity, and expected X-ray flux, for a given bolometric luminosity and redshift, assuming the standard X-ray bolometric correction from Duras et al. (2020). The tests were performed using only two bins due to the low number of candidates. There is no evidence for a signal in any of the adopted bins, suggesting the lack of a trend with either redshift or luminosity.

The significance of the detection in the UHB was also tested via simulations. We generated 1000 realizations of the type 2 sample by randomizing the position of each source, in a region within one arcmin of the original position (to ensure exposure and background levels comparable with the real sources), and repeated the stack exercise. None of the realizations returns a number of counts higher than observed. The resulting detection significance is therefore >0.999, that is, $\gtrsim 3\sigma$ (Figure 4).

To convert stacked source counts into fluxes and then luminosities, we proceed as follows. First, we assume three differ-

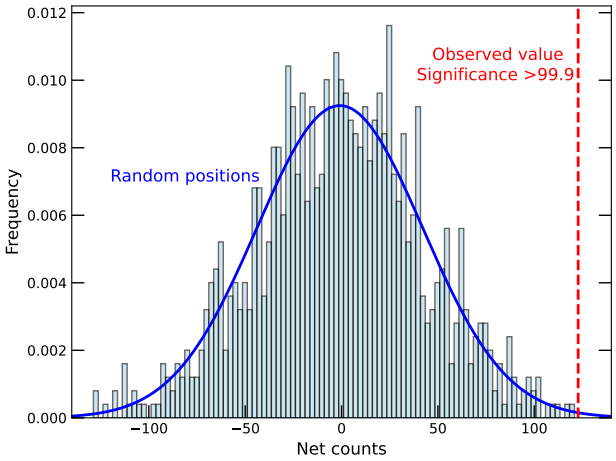

Fig. 4. Distribution of stacked net-counts in the UHB for 1000 realizations of random positions (cyan histogram). The number of stacked net counts obtained for the type 2 AGN sample is marked with the dashed red line. All of the random realizations return a lower number of net counts, implying a significance of >0.999 of the stacked emission from the type 2 AGN sample.

ent spectral models for the intrinsic emission, either a power law with $\Gamma = 2$ or a Compton-thick obscured model using the `uxclumpy` code (Buchner et al. 2019) with either $N_H = 2 \times 10^{24}$ or $N_H = 10^{25}\,\mathrm{cm}^{-2}$ (see below for details on the model parameters). Then we use an average instrumental effective area obtained from a position in the same region as the stacked sources, both for CDFS and CDFN. The response files account for the variation of *Chandra* response over time since it is computed as an average of the 102 pointings in the CDFS and the 20 pointings in the CDFN collected over time in the two fields. For each stacked object, we use its redshift to shift the intrinsic spectrum and convolve it with the effective area. This procedure allows us to obtain the expected distribution of detected photons in a given observed band corresponding to the SB, MB, and UHB rest-frame bands. We considered 1000 logarithmically spaced bins in the observed energy range 0.3–10 keV. The average expected photon energy is computed for each source and each band as $\sum(E_i \times N_i)/\sum(N_i)$, and is translated into a corresponding average effective area for that source. The sample-averaged photon energy and effective area, weighted for the effective area contributions of each source (in terms of exposure times, the contributions are roughly the same for each source), are then estimated. For example, type 2 AGN in the UHB have average photon energies in the range 1.5–4.8 keV, and average effective areas in the range 210–400 cm^2, and the sample averages are 3.3 keV and 268 cm^2, respectively. The total exposure time is computed by stacking the values at the position of each source from the exposure maps of the two fields. The fluxes are then computed, at the average observed band, as $F = (\mathrm{Counts} \times \langle E \rangle)/(T_{\mathrm{exp}} \times \langle A_{\mathrm{eff}} \rangle)$.

At the same time, the luminosities are estimated assuming the corresponding average redshift, without k-correction since the entire procedure is performed in the rest frame. Since exposures and effective areas are very different between CDFS and CDFN, the flux and luminosity limits in the CDFS and CDFN were computed separately.

The differences between fluxes and luminosities computed with an unabsorbed power-law spectrum and with a heavily absorbed one with $N_H = 2 \times 10^{24}$ or $N_H = 10^{25}\,\mathrm{cm}^{-2}$ are on the order of ∼20–30% in the SB and minimal in the MB and UHB, while they are negligible between the two Compton-thick cases; therefore, we report only the value for the $N_H = 2 \times 10^{24}$ case in Table 2.

We note that for the 1–4 keV band, a fraction of the rest-frame band moves below the *Chandra* low-energy limit of 0.3 keV for sources at $z \gtrsim 2$ (almost all our sources). When computing fluxes and luminosities, we must consider that only part of the intrinsic spectrum will be included in the observed band. We correct for this effect by computing the fraction of missing counts for each source for a given spectral shape. For example, if 70% of the intrinsic photons are expected to be missing below 0.3 keV, to recover the correct count rate the exposure time is decreased by 70%. This correction is larger for the unobscured power-law spectrum (a factor ∼2 on the final stacked flux and luminosity values) than for the Compton-thick obscuration case since the fraction of soft photons is much larger in the first case.

To estimate the spectral shape consistent with the stacking analysis results, we compared the detection in the UHB and the upper limits in the SB and MB with mock spectra for different obscuration values. The calculations used the physically motivated `uxclumpy` code (Buchner et al. 2019) in XSPEC. The model spectra cover a wide range of line-of-sight absorption column densities ($\log N_H = 20$–$26\,\mathrm{cm}^{-2}$). Two components describe the geometry of the clumpy obscuring gas. A toroidal distribution of clouds with variable vertical extent and column density parameterized by its covering factor (model parameter `TORsigma` in the range 0–0.84), plus an additional Compton-thick reflector ($\log N_H = 25.5\,\mathrm{cm}^{-2}$), which can be interpreted as part of the dust-free broad-line region, an inner rim, or a warped disk. The variable number of thick clouds parameterizes the covering factor of the ring (model parameter `CTOR` in the range 0–0.6). Given the very limited observational constraints, we fixed the slope of the primary continuum to $\Gamma = 1.9$, and the high-energy cutoff at $E_{\mathrm{cut}} = 200$ keV. We also assume a line-of-sight inclination of 60 degrees, consistent with the type 2 classification of the sample.

Model spectra were computed for a range of column densities in the high absorption regime ($\log(N_H/\mathrm{cm}^{-2}) > 23.5$), and for a range of the `TORsigma` and `CTOR` parameters. In Figure 5, we report three model spectra representative of the various possible combinations of the parameters.

The red curve refers to a spectrum transmitted through a Compton-thin ($N_H = 5 \times 10^{23}\,\mathrm{cm}^{-2}$) gas with high covering factor (0.84) and without an inner ring. The blue curve is for a Compton-thick absorber ($N_H = 2 \times 10^{24}\,\mathrm{cm}^{-2}$) with the same assumptions for the covering factor and the inner ring. The green curve includes the inner Compton-thick ring (`CTOR` = 0.6) and is for a heavily obscured, $N_H = 10^{25}\,\mathrm{cm}^{-2}$, clumpy torus with high covering factor (0.84). For sources with such large line-of-sight column densities, changes in the covering factor of the clumpy clouds (i.e., in the `TORsigma` parameter) do not significantly affect the observed spectral shape in the energy range sampled in this work.

The spectra are rescaled to the observed stacked flux in the 10–30 keV band. The upper limit in the 1–4 keV band is relatively loose, while the limit in the 4–7.25 keV band suggests that the average spectrum should steeply decline below the peak at ∼20 keV. This behavior favors Compton-thick absorption, almost independently of the details on the geometry of the clumpy absorber. Strong iron lines, with equivalent widths (EQWs) on the order of 1–2 keV, are a distinctive feature of Compton-thick absorption and are expected to contribute to the MB counts. In order to quantify their possible impact, we

Table 2. Flux and Luminosity limits.

Sample	Field	T_{exp} [Ms]		Bands		
				SB	MB	UHB
Type 1	CDFS	80.3	Flux	$<2.5 \times 10^{-18}$	$<6.7 \times 10^{-19}$	$<5.2 \times 10^{-18}$
			Lum	$<6.1 \times 10^{41}$	$<1.6 \times 10^{41}$	$<1.3 \times 10^{42}$
	CDFN	60.0	Flux	$<1.3 \times 10^{-18}$	6.6×10^{-19}	$<1.1 \times 10^{-17}$
			Lum	$<3.7 \times 10^{41}$	$<1.9 \times 10^{41}$	$<3.2 \times 10^{42}$
Type 2	CDFS	209.4	Flux	$<7.3 \times 10^{-19}$	$<1.1 \times 10^{-18}$	$1.15 \pm 0.36 \times 10^{-17}$
			Lum	$<1.4 \times 10^{41}$	$<2.1 \times 10^{41}$	$2.14 \pm 0.66 \times 10^{42}$

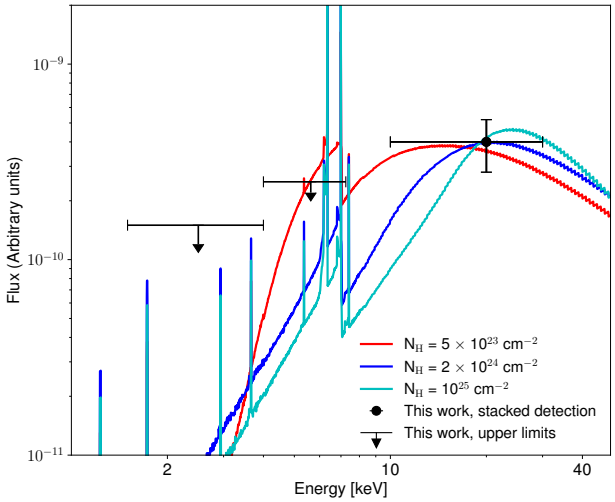

Fig. 5. Spectral models computed with the *uxclumpy* code described in (Buchner et al. 2019) rescaled to the observed 10–30 keV flux from the stacking analysis. We refer to the text for details on the model assumptions and geometry. The column density increases from 5×10^{23} cm^{-2} (red curve) to 2×10^{24} cm^{-2} (blue curve) and 10^{25} cm^{-2} (cyan curve). The UHB detection and the upper limits in the SB and MB are also reported.

also tested the staking procedure in narrower bands centered at 6.4 keV, namely 5.8–7.2 and 6.0–6.8 keV. There is no evidence for a signal with upper limits of about 20 and 10 counts, respectively. Given the *Chandra* energy resolution and the intrinsic weakness of our sources, narrower bands are severely photon starved. A putative iron K line with EQW of 2 keV at the median redshift ($z \approx 4$) of our sample would contribute to ~20% to the measured flux in the MB band. On the basis of the above-described test, we conclude that a strong iron line is fully consistent with our upper limits.

5. Discussion and conclusions

The relatively tight upper limit in the MB coupled with the UHB detection indicates the obscured nature of JWST-selected type 2 AGN. The most straightforward interpretation is that they belong to the obscured population responsible for the X-ray background spectrum (Gilli et al. 2007). In this respect, their nature is not exotic or elusive; they represent the low-luminosity tail of the AGN population, which has already been observed and characterized at lower redshifts and higher luminosities. The bolometric to X-ray luminosity ratio is shown in the left panel of Figure 6 for the type 2 sample. The magenta star corresponds to the ratio computed assuming the observed 2–10 keV luminosity for Compton-thick ($N_H = 2 \times 10^{24}$ cm^{-2}) obscuration. This model is consistent with the upper limits in the SB and MB (blue curve in Figure 5). The bolometric correction corresponding to absorption-corrected luminosities for three different values of intervening absorption is also shown with thick black marks.

The points are plotted at the median bolometric luminosity of the sample. Extreme values ($N_H \gtrsim 10^{25}$ cm^{-2}) of absorption are ruled out as they would be inconsistent with the definition of the bolometric correction. Combined with the limits obtained by the X-ray stacking, the most probable average value for the absorption is on the order of $\log N_H \sim 24.2 \pm 0.3$ cm^{-2}. This constraint is mitigated if a different recipe for calculating the bolometric correction (Netzer 2019) is adopted, as indicated by the violet star and the corresponding error bar.

We conclude that the average bolometric correction of the type 2 AGN is consistent with the values already observed in the literature, reinforcing the hypothesis that the JWST-selected type 2 AGN do not significantly differ from their lower redshift and–or higher luminosity counterparts.

For comparison, we show the location of the two X-ray-detected and X-ray-obscured sources in the parent sample: the blue diamond is XID 403 (Gilli et al. 2014), where the $k_{bol,X}$ is estimated from the observed (filled) and absorption-corrected (empty) luminosities from Circosta et al. (2019). The green diamond is GN 721, detected at ~5σ with a limited counting statistic in the CDFN (Maiolino et al. 2025). Its spectrum is flat ($\Gamma \sim 0.1$), consistent with Compton-thick obscuration. However, due to the limited number of detected photon counts, a proper spectral analysis is not possible, and therefore the $k_{bol,X}$ from the de-absorbed luminosity cannot be derived. The two candidate Compton-thick broad-line AGN could represent the tip of the iceberg of a fainter and–or more obscured population.

A question arises from their abundance. If their space densities, at present ill-constrained, turn out to be much higher than those expected based on the extrapolation of the luminosity function at high redshift, then there might be tension with the observed intensity of the hard X-ray background. However, Comastri et al. (2015) showed that the current uncertainties on the level of the X-ray background around its peak at 20–30 keV are such that it is possible to accommodate a relatively large number of heavily obscured Compton-thick AGN with a spectrum similar to those reported in Figure 5. A more detailed investigation on the space density of type 2 AGN in various JWST surveys, including the effects of incompleteness, will be the subject of a future investigation.

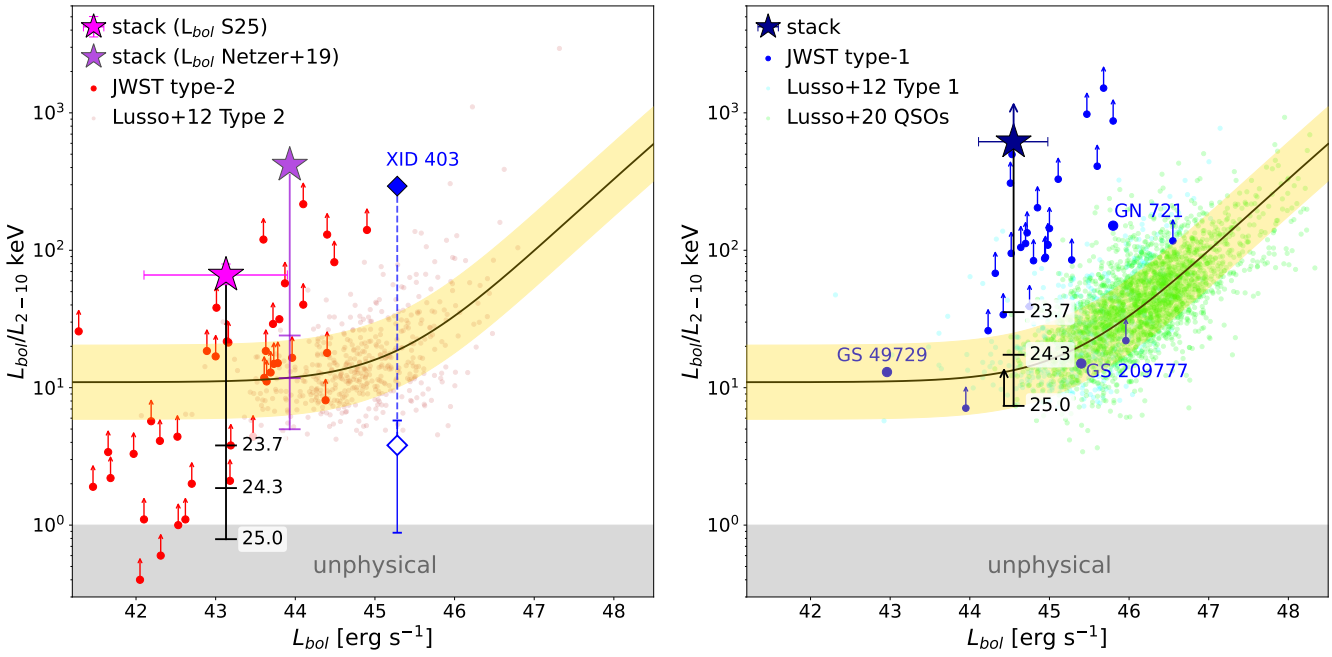

Fig. 6. *Left:* Ratio of the AGN bolometric luminosity and the X-ray luminosity as a function of the bolometric luminosity for type 2 AGN. The small brown points represent X-ray-selected type 2 AGN in COSMOS (Lusso et al. 2012). The red points are the lower limits obtained for each JWST type 2 source in M25. The magenta star shows the k_{bol} obtained from the observed 2–10 keV luminosity derived from the 10–30 keV stacked detection assuming a Compton-thick spectrum with $N_H = 2 \times 10^{24}$ cm^{-2} (blue curve in Figure 5), at the median L_{bol} of the sample. The horizontal error bar corresponds to the 16th and 84th percentiles of the observed distribution of bolometric luminosities in the stacked sample. The k_{bol} corresponding to absorption-corrected intrinsic luminosities derived for N_H of 5×10^{23}, 2×10^{24}, and 10^{25} cm^{-2} is shown with the black error bars. The violet data point is equivalent to the magenta one, but L_{bol} is derived from [O III] using the Netzer (2019) bolometric correction. The X-ray-detected heavily obscured source XID 403 is shown with a blue diamond. The $k_{bol,X}$ from the de-absorbed luminosity is shown with the empty symbol. *Right:* Same as the left panel, but for type 1 AGN. The green and cyan small points represent X-ray-selected type 1 AGN in COSMOS from Lusso et al. (2012) and QSOs from Lusso et al. (2020). The blue points are lower limits and detections for type 1 sources in M25. The dark blue star indicates the k_{bol} limit for the stacked type 1 sources in the CDFN obtained from the observed upper limits assuming a spectrum with $\Gamma = 1.7$. The black error bars were computed using the same assumptions as for the type 2 sample in the left panel. The horizontal error bar corresponds to the 16th and 84th percentiles of the observed distribution of bolometric luminosities in the stacked sample (see text for a more detailed description). In both panels, the black continuous line shows the $k_{bol,X} - L_{bol}$ relation from (Duras et al. 2020) while the gold area shows the scatter. The region below $k_{bol} = 1$ is marked as unphysical as it would imply that $L_{2-10\,keV} > L_{bol}$.

The lack of detection in any band for type 1 confirms and extends previous claims about the puzzling nature of these objects. The upper limits in the rest-frame SB, MB, and UHB are larger than those for the type 2 sample due to the shorter total exposure (140 versus 209 Msec) and the fact that the majority of the type 1 sample is in the CDFN where the exposure is lower than in the CDF-S by a factor ~3.5. The average bolometric correction for type 1 AGN in the CDFN is reported in the right panel of Figure 6[4]. The observed upper limits allow for a relatively loose constraint on the average X-ray power-law slope ($\Gamma \leq 1.7-1.8$). The blue star, plotted at the median bolometric luminosity of the sample, corresponds to the lower limit on the observed k_{bol} assuming a spectrum with $\Gamma = 1.7$. The lower limits corresponding to absorption-corrected luminosities, for the same values of intervening absorption adopted for the type 2 sample, are also reported. The observed k_{bol} lower limit for type 1 AGN is inconsistent with that measured for type 2 AGN. Heavy absorption, in the Compton-thick regime, would be needed to bring the lower limits within the region populated by the typical values of X-ray selected type 1 AGN. The X-ray weakness of type 1 AGN may be explained if these sources are accreting at rates exceeding the Eddington limit (Madau & Haardt 2024; Madau 2025). In these models, the X-ray luminosity is generated in the funnels of a geometrically thick accretion disk. The coronal plasma is cooled at lower temperatures than in standard thin disks. The emitted X-ray spectrum is extremely steep ($\Gamma \gtrsim 3-4$), making these sources undetectable, especially at high redshifts. We note that the L_{bol} range spanned by the individual data points from M25 and by our staked data points are different because the samples are different (we added new sources from J25; Zhang et al. 2025; Xiao et al. 2025, see Table A.1) and several L_{bol} values for the sources in common have been revised in J25.

A tighter constraint could be obtained by significantly increasing the sample size, especially in the CDFS. However, it should be noted that, at high redshift, the softest energies probed are on the order of a few kiloelectronvolts and thus the shape of the soft X-ray spectrum cannot be determined. As a consequence the hypothesis of an ultra-steep X-ray spectrum to explain the observed X-ray weakness (Madau & Haardt 2024) cannot be tested. Future deep and wide X-ray surveys, such as those planned by the AXIS mission concept (Reynolds et al. 2023), will probe the faint end of the luminosity function at high redshift (Marchesi et al. 2020) down to limiting fluxes one order of magnitude lower than *Chandra* deep surveys.

[4] The results for the CDFS sample are very similar, and are not reported for clarity.

Acknowledgements. We thank the anonymous referee for their constructive report. This research was supported by the Munich Institute for Astro-, Particle and BioPhysics (MIAPbP), which is funded by the Deutsche Forschungsgemeinschaft (DFG, German Research Foundation) under Germany's Excellence Strategy – EXC-2094 – 390783311. This research has made use of data obtained from the Chandra Data Archive, and software provided by the *Chandra* X-ray Center (CXC) in the application packages CIAO.

References

Ananna, T. T., Bogdán, Á., Kovács, O. E., Natarajan, P., & Hickox, R. C. 2024, ApJ, 969, L18
Baldwin, J. A., Phillips, M. M., & Terlevich, R. 1981, PASP, 93, 5
Buchner, J., Brightman, M., Nandra, K., Nikutta, R., & Bauer, F. E. 2019, A&A, 629, A16
Calabrò, A., Pentericci, L., Feltre, A., et al. 2023, A&A, 679, A80
Cappelluti, N., Li, Y., Ricarte, A., et al. 2017, ApJ, 837, 19
Circosta, C., Vignali, C., Gilli, R., et al. 2019, A&A, 623, A172
Comastri, A., Gilli, R., Marconi, A., Risaliti, G., & Salvati, M. 2015, A&A, 574, L10
D'Eugenio, F., Cameron, A. J., Scholtz, J., et al. 2025, ApJS, 277, 4
Duras, F., Bongiorno, A., Ricci, F., et al. 2020, A&A, 636, A73
Eisenstein, D. J., Johnson, B. D., Robertson, B., et al. 2025, ApJS, 281, 50
Giallongo, E., Grazian, A., Fiore, F., et al. 2015, A&A, 578, A83
Gilli, R., Comastri, A., & Hasinger, G. 2007, A&A, 463, 79
Gilli, R., Norman, C., Vignali, C., et al. 2014, A&A, 562, A67
Greene, J. E., Labbe, I., Goulding, A. D., et al. 2024, ApJ, 964, 39
Hainline, K. N., Maiolino, R., Juodžbalis, I., et al. 2025, ApJ, 979, 138
Harikane, Y., Zhang, Y., Nakajima, K., et al. 2023, ApJ, 959, 39
Hirschmann, M., Charlot, S., Feltre, A., et al. 2019, MNRAS, 487, 333
Ji, X., Maiolino, R., Ferland, G., et al. 2025, MNRAS, 541, 2134
Juodžbalis, I., Ji, X., Maiolino, R., et al. 2024, MNRAS, 535, 853
Juodžbalis, I., Maiolino, R., Baker, W. M., et al. 2025, MNRAS, submitted [arXiv:2504.03551]
Kocevski, D. D., Onoue, M., Inayoshi, K., et al. 2023, ApJ, 954, L4
Kocevski, D. D., Finkelstein, S. L., Barro, G., et al. 2025, ApJ, 986, 126
Luo, B., Brandt, W. N., Xue, Y. Q., et al. 2017, ApJS, 228, 2
Lusso, E., Comastri, A., Simmons, B. D., et al. 2012, MNRAS, 425, 623
Lusso, E., Risaliti, G., Nardini, E., et al. 2020, A&A, 642, A150
Madau, P. 2025, ApJ, submitted [arXiv:2501.09854]
Madau, P., & Haardt, F. 2024, ApJ, 976, L24
Maiolino, R., Scholtz, J., Curtis-Lake, E., et al. 2024a, A&A, 691, A145
Maiolino, R., Scholtz, J., Witstok, J., et al. 2024b, Nature, 627, 59
Maiolino, R., Risaliti, G., Signorini, M., et al. 2025, MNRAS, 538, 1921
Marchesi, S., Gilli, R., Lanzuisi, G., et al. 2020, A&A, 642, A184
Matthee, J., Naidu, R. P., Brammer, G., et al. 2024, ApJ, 963, 129
Mazzolari, G., Gilli, R., Brusa, M., et al. 2024, A&A, 687, A120
Mazzolari, G., Scholtz, J., Maiolino, R., et al. 2025, A&A, 700, A12
Moretti, A., Campana, S., Lazzati, D., & Tagliaferri, G. 2003, ApJ, 588, 696
Netzer, H. 2019, MNRAS, 488, 5185
Oesch, P. A., Brammer, G., Naidu, R. P., et al. 2023, MNRAS, 525, 2864
Pacucci, F., & Narayan, R. 2024, ApJ, 976, 96
Planck Collaboration XIII. 2016, A&A, 594, A13
Reynolds, C. S., Kara, E. A., Mushotzky, R. F., et al. 2023, SPIE Conf. Ser., 12678, 126781E
Risaliti, G., Marconi, A., Maiolino, R., Salvati, M., & Severgnini, P. 2001, A&A, 371, 37
Scholtz, J., Maiolino, R., D'Eugenio, F., et al. 2025, A&A, 697, A175
Shirazi, M., & Brinchmann, J. 2012, MNRAS, 421, 1043
Stern, J., & Laor, A. 2012, MNRAS, 423, 600
Veilleux, S., & Osterbrock, D. E. 1987, ApJS, 63, 295
Xiao, M., Oesch, P. A., Bing, L., et al. 2025, A&A, 700, A231
Xue, Y. Q., Luo, B., Brandt, W. N., et al. 2011, ApJS, 195, 10
Xue, Y. Q., Luo, B., Brandt, W. N., et al. 2016, ApJS, 224, 15
Yue, M., Eilers, A.-C., Ananna, T. T., et al. 2024, ApJ, 974, L26
Zhang, J., Egami, E., Sun, F., et al. 2025, ApJ, accepted [arXiv:2505.02895]

Appendix A: Properties of the sources used in this work

We report in this Appendix the list of sources analyzed in this work. In Table A.1 we report the sources classified as type 1, while in Table A.2 we report the sources classified as type 2. More details on the sample selection criteria are reported in Section 2.

Table A.1. Type 1 AGN sample.

ID	RA	DEC	z	$\log(\frac{L_{bol}}{L_{\odot}})$	Reference
159438	53.0544714	-27.902462	3.239	44.11	J25
9598	53.1618083	-27.7707168	3.324	43.85	J25
17341	53.0872694	-27.7296227	3.598	44.01	J25
179198	53.0889771	-27.8606946	3.830	43.92	J25
13329	53.1390379	-27.7844332	3.936	44.11	J25
172975	53.0877297	-27.8712419	4.741	44.07	J25
8083	53.1328431	-27.8018578	4.648	44.03	J25
38562	53.1358639	-27.871645	4.822	44.70	J25
159717	53.0975283	-27.9012603	5.077	45.13	J25
204851	53.1385932	-27.7902534	5.480	44.97	J25; 13971 in M25
3073	53.078875	-27.884156	5.55	45.68	M25
10013704	53.1265350	-27.8180923	5.919	44.29	J25
30148179	53.142082	-27.779848	5.922	44.25	J25
210600	53.1661147	-27.7720397	6.306	44.29	J25
3608	189.117958	62.235528	5.269	43.95	M25
4014	189.300125	62.212028	5.228	44.95	M25
9771	189.281000	62.247306	5.538	45.80	M25
12839	189.344292	62.263361	5.241	45.47	M25
13733	189.057083	62.268917	5.236	44.70	M25
14409	189.072083	62.273417	5.139	44.85	M25
15498	189.285542	62.280778	5.086	45.00	M25
16813	189.179292	62.292528	5.355	44.94	M25
z11	189.106083	62.242056	10.604	44.98	M25
LRD1	189.019240	62.243531	7.0388	...	Xiao et al. (2025)
LRD2	189.083488	62.202579	7.1883	...	Xiao et al. (2025)
1085355	189.094365	62.198974	4.88	44.69	Zhang et al. (2025)
1008671	189.161845	62.251054	4.41	44.86	Zhang et al. (2025)
1029154	189.159025	62.260221	4.17	44.69	Zhang et al. (2025)
1033320	189.125779	62.287404	4.48	44.42	Zhang et al. (2025)
1034620	189.159764	62.295924	5.19	44.98	Zhang et al. (2025)
1082263	189.212584	62.227436	3.98	44.55	Zhang et al. (2025)
1086784	189.305706	62.236946	4.40	44.53	Zhang et al. (2025)
1086855	189.286512	62.238138	4.41	44.86	Zhang et al. (2025)
1087315	189.333584	62.246178	3.91	44.47	Zhang et al. (2025)
1089568	189.151821	62.272229	4.05	44.58	Zhang et al. (2025)
1090549	189.235941	62.285544	5.20	44.57	Zhang et al. (2025)
1008411	189.211089	62.250271	4.41	44.49	Zhang et al. (2025)
77652	189.293228	62.199003	5.229	44.11	J25
73488	189.197396	62.177233	4.133	45.22	J25
62309	189.248977	62.218350	5.172	43.56	J25
61888	189.168016	62.217013	5.874	44.38	J25
53757	189.269778	62.194208	4.447	44.29	J25
38509	189.09144	62.22811	6.68	44.84	J25; 1146115 in M25
29648	189.209198	62.264268	2.959	43.90	J25
28074	189.064576	62.273820	2.259	45.76	J25
20621	189.122515	62.292850	4.682	44.17	J25
11836	189.220587	62.263675	4.409	44.11	J25
2916	189.107739	62.269525	3.664	43.91	J25
1093	189.179742	62.224629	5.594	44.32	J25
954	189.151966	62.259635	6.759	45.17	J25

Table A.2. Type 2 AGN sample.

ID	RA	DEC	z	$\log(\frac{L_{bol}}{L_\odot})$	Reference
GS 10040620	53.116542	-27.762060	1.776	41.63	S25
GS 8456	53.126083	-27.800690	1.884	41.56	S25
GS 209979	53.173542	-27.773750	1.883	42.68	S25
GS 10036017	53.105958	-27.808470	2.016	44.08	S25
GS 10012511	53.120500	-27.762750	2.019	41.66	S25
GS 10008071	53.154458	-27.771440	2.227	43.12	S25
GS 8880	53.127250	-27.799310	2.327	41.95	S25
GS 17670	53.125083	-27.775720	2.350	42.99	S25
GS 10073	53.113333	-27.795580	2.632	42.98	S25
GS 10011849	53.120042	-27.777860	2.686	43.58	S25
GS 7099	53.113792	-27.805220	2.860	42.87	S25
GS 114573	53.114750	-27.795970	2.881	42.28	S25
GS 111511	53.154000	-27.800920	3.008	42.50	S25
GS 132213	53.158542	-27.772110	3.012	42.17	S25
GS 10013597	53.123250	-27.769390	3.320	42.60	S25
GS 10035295	53.114333	-27.815500	3.588	43.70	S25
GS 104075	53.107042	-27.812030	3.717	43.14	S25
GS 108487	53.148875	-27.805670	3.975	41.91	S25
GS 7762	53.113333	-27.803000	4.146	43.62	S25
GS 95256	53.148958	-27.822580	4.159	42.08	S25
GS 10000626	53.147000	-27.813030	4.468	42.51	S25
GS 111091	53.111667	-27.801610	4.497	42.03	S25
GS 17072	53.170208	-27.777390	4.707	42.29	S25
GS 10015338	53.115333	-27.772890	5.073	43.85	S25
GS 4902	53.11852484	-27.81296696	5.123	43.0	S25
GS 9452	53.115833	-27.797560	5.135	43.59	S25
GS 202208	53.164083	-27.799720	5.450	44.88	S25
GS 208643[a]	53.130208	-27.778360	5.566	43.61	S25
GS 16745[a]	53.130042	-27.778389	5.574	43.7	S25
GS 22251	53.154083	-27.766080	5.804	44.08	S25
GS 10056849	53.113500	-27.772830	5.820	43.16	S25
GS 201127	53.166833	-27.804140	5.837	43.45	S25
GS 99671	53.126625	-27.817720	5.936	43.17	S25
GS 9422	53.121750	-27.797640	5.942	44.47	S25
GS 10013609	53.117292	-27.764080	6.931	43.94	S25
GS 10013905	53.118333	-27.769000	7.206	43.67	S25
GS 21842	53.156833	-27.767170	7.981	43.76	S25
GS 10058975	53.112417	-27.774610	9.436	44.36	S25

Notes. [a] These two sources are at the same position (within the *Chandra* psf) and at very similar redshift, and are therefore counted only once in the stack.